UHASSELT

KNOWLEDGE IN ACTION

Faculteit Wetenschappen

master in materiomics

Masterthesis

Tailoring the Au size and loading of plasmonic Au/CeO_{2x} catalysts for the light-powered reverse water gas shift reaction

Romy van Geijn

Scriptie ingediend tot het behalen van de graad van master in materiomics

PROMOTOR :

Prof. dr. Pascal BUSKENS

Prof. dr. Marlies VAN BAEL

2024
2025

UHASSELT

KNOWLEDGE IN ACTION

www.uhasselt.be
Universiteit Hasselt
Campus Hasselt:
Martelarenlaan 42 | 3500 Hasselt
Campus Diepenbeek:
Agoralaan Gebouw D | 3590 Diepenbeek

UHASSELT

KNOWLEDGE IN ACTION

Faculteit Wetenschappen

master in materiomics

Masterthesis

Tailoring the Au size and loading of plasmonic Au/CeO_{2x} catalysts for the light-powered reverse water gas shift reaction

Romy van Geijn

Scriptie ingediend tot het behalen van de graad van master in materiomics

PROMOTOR :

Prof. dr. Pascal BUSKENS

Prof. dr. Marlies VAN BAEL

Tailoring the Au size and loading of plasmonic Au/CeO_{2-x} catalysts for the light-powered reverse water gas shift reaction

Romy van Geijn[1,], Esmee Roman[1,2,3], Marcel Verheijen[4,5], Ken Elen[1,2,3], Daniel Mann[1,6], Marlies van Bael[1,2,3]and Pascal Buskens[1,6]*

[1]Institute for Materials Research (imo-imomec), DESINe Group, Hasselt University, Agoralaan Building D, 3590 Diepenbeek, Belgium.

[2]IMOMEC Associated Laboratory, IMEC vzw, Wetenschapspark 1, 3590 Diepenbeek, Belgium.

[3]EnergyVille, Thor Park 8320, 3600 Genk, Belgium.

[4]Department of Applied Physics, Eindhoven University of Technology, Eindhoven 5600 MB, The Netherlands

[5]Eurofins Materials Science, High Tech Campus 11, Eindhoven 5656 AE, The Netherlands

[6]The Netherlands Organisation for Applied Scientific Research (TNO), Eindhoven, The Netherlands.

[*]Corresponding authors. E-mail: romy.vangeijn@student.uhasselt.be

Keywords: reverse water gas shift, syngas, localized surface plasmon resonance, photocatalysis, gold, ceria

Abstract (EN): This thesis explores the synthesis, characterization, and photocatalytic performance of plasmonic Au/CeO_{2-x} catalysts for the reverse water gas shift (rWGS) reaction. Phase-pure CeO_{2-x} was synthesized using both static and rotating hydrothermal methods, resulting in similar particle sizes and crystallinity. Gold nanoparticles were deposited via a Sn^{2+}-assisted seeded growth method, yielding uniformly dispersed Au particles below 7 nm. Systematic variation of Au and Sn precursor concentrations revealed that the gold loading could be tuned, while the particle size remained largely unaffected. Catalytic testing demonstrated that illumination significantly enhances CO production. Although activity increased under light and heat, the synthesized catalysts were less active than reference Au/CeO_{2-x} and Au/TiO_2 systems, possibly due to excessive Sn coverage limiting access to oxygen vacancies and Ce^{3+}

sites. Additionally, one catalyst (S7-S) showed signs of instability after reaction, indicated by a colour change and changes in optical properties.

Abstract (NL): In dit onderzoek zijn plasmonische Au/CeO_{2-x}-katalysatoren gesynthetiseerd, gekarakteriseerd en getest voor de lichtgedreven reverse water gas shift (rWGS)-reactie. Fasepuur CeO_{2-x} werd succesvol bereid via zowel statische als roterende hydrothermale synthese, waarbij vergelijkbare deeltjesgroottes en kristalliniteit werden verkregen. Goud nanodeeltjes (< 7 nm) werden afgezet via een Sn^{2+}-geassisteerde 'seeded growth'-methode, wat zorgde voor een gelijkmatige verdeling van goud op het oppervlak. Door systematische variatie van de Au- en Sn-precursorgehaltes kon de goudbelading effectief worden aangepast, terwijl de grootte van de gouddeeltjes grotendeels constant bleef. Katalytische testen toonden aan dat CO-productie aanzienlijk toeneemt onder gelijktijdige verhitting en belichting. De katalytische activiteit bleef echter lager dan die van referentiekatalysatoren op basis van Au/CeO_{2-x} en Au/TiO_2, mogelijk als gevolg van overmatige Sn-bedekking die actieve plaatsen (Ce^{3+} en zuurstofvacatures) op het oppervlak afschermt. Eén katalysator (S7-S) vertoonde na reactie een kleurverandering en spectrale verschuivingen, wat wijst op mogelijke instabiliteit. Deze bevindingen benadrukken het belang van een gebalanceerde Sn-concentratie voor zowel prestaties als structurele stabiliteit van Au/CeO_{2-x}-katalysatoren.

1. Introduction

Reducing carbon dioxide (CO_2) emissions has emerged as one of the most pressing challenges in addressing climate change.[1] Closing the carbon cycle by converting CO_2 back into fuels can help reduce CO_2 levels in the atmosphere and allow CO_2 to be reused. Incorporating carbon capture and utilisation (CCU) strategies can help capture emissions and turn them into valuable products, contributing to a more sustainable carbon economy.[2] Carbon monoxide (CO) is, for instance, a valuable chemical building block used, together with H_2 as syngas, in the synthesis of fuels and chemicals.[3] Albeit, CO_2 is relatively inert and chemically stable due to its linear structure with strong double bonds between carbon and oxygen atoms, making its conversion to the more reactive CO an energy-intensive process. Efforts to convert CO_2 into useful products have gained significant attention, with the reverse water-gas shift (rWGS) reaction (Eq. 1) being one of the most promising reactions for converting CO_2 into CO.[4]

rWGS $\quad \mathrm{CO_2 + H_2 \leftrightarrows CO + H_2O} \quad \Delta H_{298K} = +41.2\ \mathrm{kJ\ mol^{-1}}$ (1)

Sabatier reaction $\mathrm{CO_2 + 4H_2 \rightarrow CH_4 + 2H_2O} \quad \Delta H_{298K} = -165.0\ \mathrm{kJ\ mol^{-1}}$ (2)

The thermally induced catalytic rWGS reaction is thermodynamically challenging since it is an endothermic process with equilibrium limitations. Below 600 °C, methane (CH_4) is the primary product generated by the exothermic Sabatier reaction (Eq. 2). To achieve CO selectivity, the rWGS reaction typically requires temperatures above 600°C, which thus competes directly with the methanation reaction. However, these high-temperature conditions pose several challenges, including catalyst deactivation due to coke formation and sintering.[5–7]

Photocatalysis, which harnesses the energy of sunlight to perform the rWGS reaction under near-ambient conditions, presents an attractive lower-temperature replacement for high-temperature thermal catalysis. Within photocatalysis, semiconductor-based photocatalysts have been widely studied for their ability to generate charge carriers upon light absorption and subsequently drive chemical reactions.[8] However, their absorption range restricts their efficiency, especially since stable oxidic semiconductors primarily operate in the UV region (~4% of the solar spectrum). To improve this, recent research has focused on incorporating plasmonic metallic nanoparticles (NPs), which play a significant role in plasmon catalysis. These NPs enhance visible light absorption through localized surface plasmon resonance (LSPR), a collective oscillation of conduction electrons in metal NPs when excited by light at their interface with the surrounding environment.[6]

LSPR can boost reaction yields and improve spatial precision by enabling targeted activation of specific areas within a reaction mixture, and enhance temporal precision by allowing for precise control over the timing and duration of reactions. LSPR in semiconductor supported metallic nanoparticle catalysts produces four key effects that are highly advantageous for the activation of reactants:[9]

(1) Excitation of hot charge carriers, where the energy from LSPR promotes electrons to higher energy states, resulting in the injection of hot electrons into the antibonding orbitals of neighbouring reagent molecules. When a plasmonic nanoparticle is attached to a semiconductor, hot electrons can cross the Schottky barrier into the conduction band, prolonging the charge carrier lifetime and enhancing their likelihood of participating in catalytic reactions.

(2) Heat generation due to the Joule effect (ohmic losses), which increases the catalyst's surface temperature, accelerating reaction kinetics.

(3) Conventional UV-induced electron-hole pair generation in semiconductors.

(4) Near-field enhancement where light is concentrated at specific positions on the NP surface depending on particle morphology, leading to an increase in the local density of photons

per unit volume. The near-field enhancement effect can significantly enhance photo-activated processes or generate additional charge carriers when combined with a semiconductor.[5–7]

This combination of non-thermal contributors (1,3 and 4) and photothermal heating (2) provides new opportunities to control and enhance chemical processes.[9] The size of plasmonic NPs significantly affects LSPR, making their deposition on supporting materials to maintain their small size a necessity.[6] These supports not only hold the NPs but also boost the catalyst's surface chemistry by improving the adsorption and activation of reactants critical for CO_2 conversion. Additionally, the electronic properties of the support can modify the catalyst's optical characteristics, facilitating solar energy capture.

Numerous research groups have investigated plasmonic NP catalysts supported on a variety of materials for facilitating the solar-powered rWGS reaction, with Au NPs supported on metal oxides as most promising candidates.[5–8] Au exhibits strong LSPR properties and can catalyse the rWGS reaction under visible light irradiation. A photocatalyst consisting of Au NPs on CeO_{2-x} nanorods has been shown to achieve a CO production rate ten times higher under photocatalytic conditions compared to thermal catalysis.[10] This increased activity is attributed to plasmon-assisted hydrogen splitting on the Au surface, highlighting the divergence in performance under different experimental conditions. Another study compared various supports and found that the Au/CeO_{2-x} photocatalyst exhibited the highest light/dark enhancement compared to Au/TiO_2 and Au/Al_2O_3.[11] For Au/TiO_2, this was explained by a carboxyl-mediated associative mechanism at the Au/TiO_2 interface, where LSPR enhances carboxyl decomposition or hydroxyl hydrogenation. Literature indicates that smaller gold particles can exhibit enhanced catalytic activity compared to larger ones due to their higher surface area-to-volume ratio and increased number of active sites.[6] Ceria, a n-type semiconductor, plays a crucial role in stabilizing the gold nanoparticles and providing oxygen vacancies (V_Os), which enhance the activation and conversion of CO_2.[12] Its face-centered cubic (FCC) fluorite structure is typically non-stoichiometric, as oxygen vacancies readily form under reducing conditions.[13,14] These vacancies are charge-compensated by the reduction of Ce^{4+} to Ce^{3+}, while the crystal structure remains intact. V_Os are reversible under oxidizing conditions

Despite the progress made in Au NP-supported plasmonic photocatalysis, significant knowledge gaps remain, particularly regarding the precise role of particle size, distance and shape, and in modulating the LSPR and enhancing catalytic activity. Size is a crucial factor in plasmonic catalysis.[15] Smaller nanoparticles (NPs) have a higher surface-area-to-volume ratio, which increases catalytic activity. Additionally, the balance between absorption and scattering

is size-dependent, with absorption being important for generating hot electrons and holes. This affects the efficiency of plasmonic catalysis. To study size effects accurately, nanoparticles with controlled sizes within an optimal range are needed, but achieving this control is challenging. For spherical nanoparticles, this size dependence is relatively weak.[16] As a result, spherical nanoparticles exhibit only limited variation in their resonance frequency, allowing them to absorb only a small portion of the visible solar spectrum. A way to tune the resonance frequency is by changing the geometry of the NPs from spheres to e.g. plates (disks). For plate-like structures, the resonance frequency is influenced by the plate's thickness, width and surface area.[16]

To our knowledge, the effect of Au nanoparticle size and loading on the performance of plasmonic Au/CeO_2 catalysts in the sunlight-driven rWGS reaction has not been thoroughly studied. Therefore, this study aims to fill these gaps by synthesizing and characterizing a range of Au/CeO_{2-x} catalysts with controlled particle size and loading. UV-vis-NIR spectrophotometry will be used to study LSPR behaviour and catalytic testing will assess the impact of Au particle size and loading on the catalytic performance in the light-powered rWGS reaction.

2. Experimental methods

2.1 Hydrothermal synthesis of CeO_{2-x}

CeO_{2-x} particles were synthesised via a hydrothermal method adapted from Volders et al.[12] In a standard synthesis, cerium(III) nitrate hexahydrate ($Ce(NO_3)_3 \cdot 6H_2O$; 4.397 g, 10.12 mmol; Thermo Scientific Chemicals, 99,5%) and polyvinylpyrrolidone (PVP; 2.490 g, 22.4 mmol monomer units; average molecular weight 8,000; Acros Chemicals) were dissolved in an 81 mL solvent mixture of ethanol (27 ml, VWR Chemicals, 99.8%) and ultrapure water (54 ml, Milli-Q, Millipore, Billerica, MA, USA; 18.2 MΩ·cm) in a 100 mL beaker fitted with a lid.

The solution was sonicated for two minutes in an ultrasonic bath (Fisherbrand, FB15057) to facilitate PVP dissolution, and subsequently stirred using a magnetic stirrer under ambient conditions for one hour, with the beaker remaining covered. The mixture was then divided equally among three Teflon-lined stainless steel autoclaves (Parr Instrument Company, Model 4744, 45 mL capacity), with 27 mL transferred into each vessel.

Hydrothermal treatment was performed at 160 ºC for 20 hours in a convection oven (Binder, ED series 53) either under static (S) conditions or with rotation (R). After completion, the autoclaves were allowed to cool naturally to room temperature within the oven. The rotating experiments were conducted to assess whether variation in particle size could be reduced

compared to the results reported in the study by Volders et al.[12] The resulting dispersions were centrifuged (10000 rpm, 5 minutes, 20 ºC) three times with ultrapure water and once with ethanol to remove residual soluble species. The collected solids were subsequently dried overnight under ambient conditions. After drying, the remaining material was ground using a mortar and pestle to obtain a fine powder suitable for thermal treatment.

The obtained powders were subjected to calcination in flowing dry air at 400 ºC for two hours in an alumina crucible, using a heating rate of 3.1 ºC min^{-1} and an air flow rate of 0,6 L min^{-1}. This thermal treatment removed residual organic compounds and yielded a white to pale yellow CeO_{2-x} powder. The samples were cooled to room temperature inside the tube furnace.

To reduce the effect of variability between synthesis batches, materials from repeated preparations were combined before continuing with the following synthesis steps. Static and rotating samples, however, were processed independently and not combined at any stage.

2.2 Au seeding on CeO_{2-x} support

Au/CeO_{2-x} particles were synthesised via a seeding method adapted from Mann et al.[16] In a typical procedure, CeO_{2-x} particles were dispersed in ultrapure water (Milli-Q, Millipore, Billerica, MA, USA; 18.2 MΩ·cm) and added to an aqueous solution containing tin(II) chloride ($SnCl_2$; 98%, Honeywell Research Chemicals), hydrochloric acid (HCl, 37%, VWR Chemicals), and additional ultrapure water, with ratios detailed in **Table 1** and Supporting Information (SI) 1: Au seeding on CeO_{2-x} support. The resulting mixture was stirred at room temperature for one hour to facilitate the deposition of tin species onto the CeO_{2-x} surface.

The dispersion was centrifuged (10,000 rpm, 5 min, 20 ºC) three times with ultrapure water, after which the resulting pellet was redispersed in ultrapure water using an ultrasonic bath to ensure complete homogenisation. The pH of the Sn/CeO_{2-x} dispersion was then adjusted to 6 by the slow addition of 1 M aqueous ammonia, prepared from concentrated ammonia solution (25%, VWR Chemicals), under continuous stirring.

The Sn/CeO_{2-x} dispersion was added to a solution of gold(III) chloride hydrate ($HAuCl_4 \cdot xH_2O$, 99,995% trace metals basis, Sigma-Aldrich) and potassium carbonate (K_2CO_3, ≥99.0%, Sigma-Aldrich) in ultrapure water. Formaldehyde solution (CH_2O; 37%, Merck) was subsequently added as the reducing agent. The mixture was stirred and heated to 80 ºC for one hour. Following the reaction, the dispersion was cooled to room temperature and centrifuged (10,000 rpm, 5 min, 20 ºC) three times with ultrapure water to remove residual soluble species. The resulting wet Au/CeO_{2-x} pellet was dried overnight at 80 ºC in a convection oven (Binder, ED series 53) to obtain a dry powder, which was subsequently ground using a mortar and pestle.

Table 1. The different Au seeding synthesis with the theoretical gold content and equivalents of CeO_{2-x}, $SnCl_2$ and $HAuCl_4 \cdot x\ H_2O$. More information see SI 1.

Au seeding	Wt% Au	Eq CeO_{2-x}	Eq $SnCl_2$	Eq $HAuCl_4 \cdot x\ H_2O$
S1	5.5	1.0	0.76	0.05
S2	5.5	1.0	0.77	0.05
S3	5.5	1.0	0.77	0.05
S4	2.9	1.0	0.39	0.03
S5	6.9	1.0	0.97	0.06
S6	5.5	1.0	1.54	0.05
S7	5.5	1.0	4.30	0.05

2.3 Characterization

Transmission electron microscopy (TEM) analysis of the CeO_{2-x} particles was carried out using a FEI Tecnai Spirit transmission electron microscope operated at an accelerating voltage of 120 kV. The powder samples were first dispersed in ethanol and sonicated for one minute. Subsequently, five droplets of the suspension were deposited onto a TEM grid and allowed to dry under a lamp prior to imaging. The particle size of CeO_{2-x} was determined using MATLAB in combination with the CircleFinder package, based on the analysis of at least 50 particles across multiple TEM images. Scale bars were measured in pixels, and the extracted particle sizes were subsequently converted to nanometres.

High-resolution imaging of the Au/CeO_{2-x} catalysts was carried out using a JEOL ARM 200F transmission electron microscope equipped with a probe corrector and operated at 200 kV. Microstructural characterisation was performed in high-angle annular dark-field scanning transmission electron microscopy (HAADF-STEM) mode. Elemental composition was assessed via energy-dispersive X-ray spectroscopy (EDX) using a Centurio silicon drift detector (100 mm^2 active area). For EDX mapping, full spectral data were acquired over 256 x 256 pixel grids at varying magnifications. To minimise electron beam damage, 50-100 frames were recorded and summed per map, with a dwell time of 0.1 ms per pixel per frame. The resulting maps were used for elemental identification, and particle size distributions were determined from the associated HAADF-STEM micrographs recorded under consistent magnification conditions. The particle size of the Au nanoparticles was determined manually using ImageJ (Fiji), by measuring at least 40 individual particles across multiple STEM-EDX images. Scale bars were converted to pixel units, and the measured particle sizes were subsequently expressed in nanometres.

Diffuse reflectance UV-Vis spectroscopy was carried out using a Cary UV-Vis-NIR spectrometer (Agilent Technologies). A polytetrafluoroethylene (PTFE) reference was used to

establish the baseline corresponding to 100% reflectance, while the zero-reflectance point was defined in the absence of the sample holder. For each measurement, ~2 mg of sample was thoroughly mixed with ~500 mg of potassium bromide (KBr; Uvasol®, Merck, for IR spectroscopy) and loaded into the sample holder. Reflectance spectra were recorded in scan mode over the 300-800 nm wavelength range at a scan rate of 10 nm/s.

The gold content in the Au/CeO_{2-x} catalysts was quantified by inductively coupled plasma–optical emission spectrometry (ICP-OES) using a PerkinElmer Optima 330 DV simultaneous spectrometer (PerkinElmer, Waltham, MA, USA). Prior to analysis, the samples were digested in a Milestone microwave digestion system using 10 mL of a mixed acid solution comprising hydrochloric acid (≥37%, TraceSELECT, Honeywell Chemicals), nitric acid (69.0–70.0%, J.T. Baker), and hydrofluoric acid (40%, AnalaR NORMAPUR®, VWR) in a volume ratio of 3.17:1:1.71, respectively. For calibration, a 1000 ppm gold standard solution (Merck) was diluted to prepare 1, 2, 5, and 10 ppm standards in 5% HNO_3. Sample solutions were similarly diluted to final concentrations of 1 or 10 ppm. All measurements were performed in triplicate to ensure reproducibility.

Powder X-ray diffraction (XRD) analysis was performed using a Bruker D8 diffractometer equipped with Cu Kα radiation (λ = 1.5406 Å). Data were collected in reflection mode over a 2θ range of 10º to 130º, with a step size of 0.05º and a counting time of 0.6 seconds per step.

2.4 Plasmon catalysis

Catalytic tests were conducted using a custom-designed reactor equipped with a quartz window at the top to enable light irradiation. Approximately 80 mg of catalyst was homogeneously distributed onto a quartz filter (Whatman QM-A filter discs, 2.2 µm pore size, quartz) positioned within the irradiated area, which measured approximately 2.14 cm^2. Illumination was provided by a 300 W xenon arc lamp (LOT-Quantum Design, LSB531), delivering an intensity equivalent to approximately 9 suns.

In a typical experiment, the catalyst was loaded into the reactor, which was subsequently evacuated and purged before being filled with a gas mixture consisting of hydrogen (H_2; Air Liquide, P0232), carbon dioxide (CO_2; Air Liquide, P1209), and nitrogen (N_2; Air Liquide, P0271) at flow rates of 8 mL min^{-1}, 8 mL min^{-1}, and 4 mL min^{-1}, respectively. The reactor pressure was maintained at 3.5 bar using a backpressure regulator.

Prior to the start of each experiment, three gas chromatograph GC runs were performed to purge the system and ensure complete removal of excess O_2 from the reactor. The xenon lamp was switched on to preheat the system concurrently with the activation of the gas

chromatograph without illumination of the catalyst. Each experiment followed a stepwise procedure: 30 minutes of light irradiation alone, followed by 30 minutes of simultaneous irradiation and heating at 150 °C, then 30 minutes at 250 °C with continued irradiation, and finally 30 minutes of thermal treatment at 250 °C in the absence of light. Reaction products were analysed using an Agilent 990 Micro GC equipped with two thermal conductivity detector channels: an MS5A stainless steel column for the detection of H_2, O_2, N_2, CH_4, and CO, and a PORAPLOT U column for CO_2 and higher hydrocarbons (C_2^+). Peak areas were converted to concentrations in ppm using calibration curves, with N_2 used as the internal standard.

3. Results and discussion

3.1. CeO_{2-x} synthesis: rotating vs. static

Two distinct hydrothermal synthesis approaches were employed to synthesise CeO_{2-x}: one conducted under rotating (R) conditions and the other under static (S) conditions, with multiple syntheses performed for each approach.

TEM images show that the CeO_{2-x} particles exhibit a predominantly spherical morphology, though slight faceting at the edges gives them a more squared-spherical appearance for both the rotating and static (**Figure 1a/b** and SI 2 **Figure S5**). The images shown correspond to synthesis 3 for each condition, while additional images from the other syntheses are included in the Supporting Information. Particle size analysis, based on TEM measurements across all three syntheses per approach, revealed average particle sizes of 121.1 ± 1.13 nm for R-CeO_{2-x} and 119.7 ± 4.95 nm for S-CeO_{2-x}, representing aggregates composed of smaller crystallites. While the mean particle size remained comparable between the two conditions (~120 nm), the standard deviation was markedly lower in the rotating synthesis. This suggests that autoclave rotation promotes a narrower particle size distribution, likely due to enhanced homogeneity in temperature and solute transport during the hydrothermal process. Notably, these results represent a substantial reduction in both average size and variability when compared to the static hydrothermal synthesis reported by Volders et al.[12], which yielded particles of 196 ± 13 nm. The use of a smaller autoclave in the present study, for both static and rotating conditions, may also have contributed to the observed reduction in particle size, as smaller reaction volumes generally allow for more uniform heat and mass transfer, promoting controlled nucleation and limiting particle overgrowth.

The powder XRD patterns of all CeO_{2-x} samples synthesised under static and rotating hydrothermal conditions exhibit a series of peaks that are consistent with the cubic fluorite structure (Fm-3m) of cerium dioxide (CeO_2), as indexed by JCPDS 65-5923 (**Figure 1c** and SI

6 **Figure S10**). The diffractograms shown correspond to synthesis 3 under both static and rotating conditions, while additional diffractograms from the other syntheses are provided in the Supporting Information. The most intense reflection occurs at $2\theta \approx 28.5^{\circ}$, corresponding to the (111) plane. Additional peaks observed at approximately 33.1º (200), 47.5º (220), 56.3º (311), 59.1º (222), 69.4º (400), and 76.7º (331) further confirm the formation of phase-pure CeO_2.[17–19] A small peak near $2\theta \approx 44^{\circ}$, present in almost all patterns, originates from the sample holder. In conclusion, no secondary phases or impurities were detected, and no discernible shift in peak positions was observed between static and rotating syntheses, indicating that the crystallographic structure remains unaffected by the rotation. The crystallite sizes of the statically and rotationally synthesized CeO_{2-x} samples were calculated using the Scherrer equation based on the (111) diffraction peak at $2\theta \approx 28.5^{\circ}$. The statically synthesized samples exhibited an average size of 20.28 ± 1.51 nm, while the rotationally synthesized samples measured 19.75 ± 1.72 nm. The small difference falls within the range of experimental uncertainty. Under the given synthesis conditions, rotation does not appear to significantly affect crystallite size.

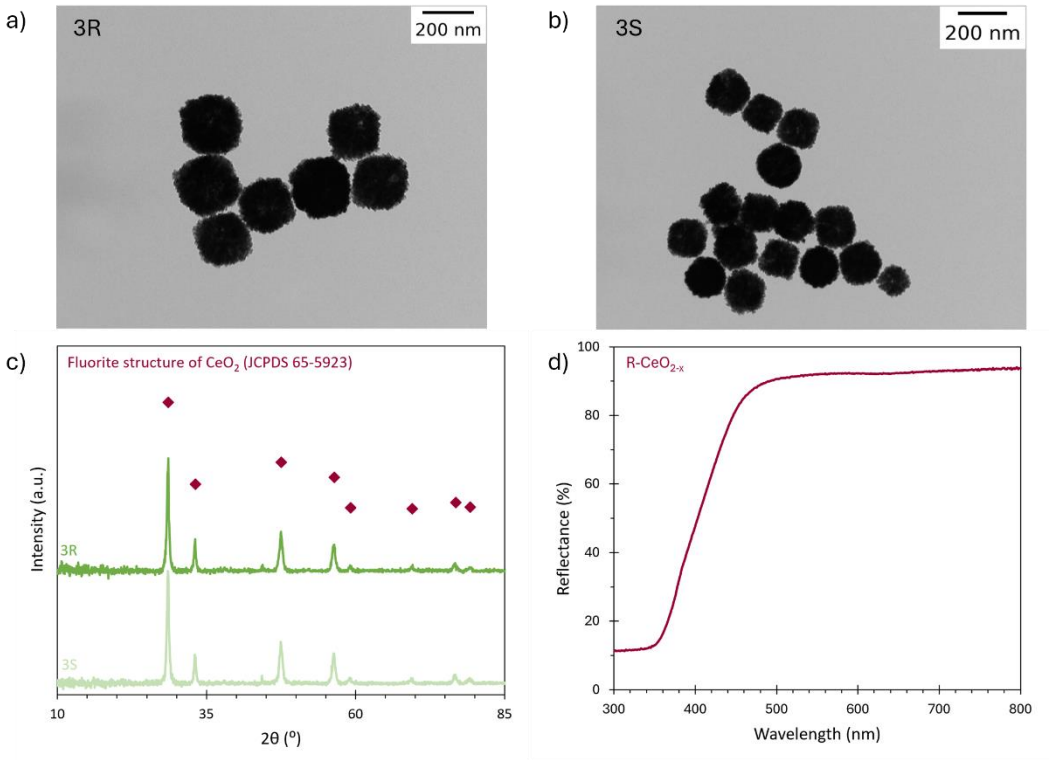

Figure 1. a) TEM image of 3R-CeO_{2-x} particles. b) TEM image of 3S-CeO_{2-x} particles. c) XRD diffractogram of 3S and 3R are shown, where the numerical prefix indicates the synthesis batch. Samples sharing the same number correspond to static and rotating syntheses derived from the same precursor batch. A minor peak observed at approximately 44º 2θ originates from the sample holder and is not associated with the CeO_{2-x} phase. d) Diffuse reflectance UV-Vis spectra of a mix of R-CeO_{2-x}.

Diffuse reflectance UV-Vis spectroscopy was performed to evaluate the optical properties of the R-CeO_{2-x} sample (**Figure 1d**). The spectrum displays a sharp increase in reflectance beginning around 400 nm, which is characteristic of the intrinsic band gap absorption of CeO_{2-x}. This edge corresponds to the transition from the valence band (O 2p) to the localized Ce 4f states near the conduction band, and is typically associated with a band gap in the range of 3.0-3.2 eV, consistent with reported values for ceria.[20,21] The optical band gap of the R-CeO_{2-x} particles is estimated using Tauc analysis of the diffuse reflectance UV-Vis data (SI 3 **Figure S6**). Assuming an indirect allowed transition, the Tauc plot was constructed by plotting $(F(R)hv)^{1/2}$ against photon energy (hv), where $F(R)$ is the Kubelka-Munk function. The band gap energy is determined from the intercept of the extrapolated linear portion of the absorption edge with the x-axis, yielding a value of approximately 3.0 eV.

3.2. Gold seeding on ceria support

Gold was deposited onto both S- and R-CeO_{2-x} supports using a seeded growth method involving chemical reduction. In this procedure, Sn^{2+} ions introduced via $SnCl_2$ were first adsorbed onto the CeO_{2-x} surface to create defined nucleation sites. These Sn-modified surface regions enhance the chemical affinity for Au^{3+} species and facilitate site-selective gold nucleation. Upon the subsequent addition of formaldehyde, Au^{3+} ions from $HAuCl_4$ are reduced to metallic Au^0 and preferentially deposit at Sn-enriched sites, resulting in improved dispersion and control over particle formation. The introduction of Sn^{2+} also alters the redox environment at the ceria surface. Sn^{2+} donates electrons to the ceria lattice, leading to partial reduction of Ce^{4+} to Ce^{3+} and the formation of oxygen vacancies.[22,23] This redox interaction may influence the density of oxygen vacancies and electronic properties of the support, which are critical parameters in catalytic performance (next section). To investigate the influence of synthesis parameters on gold loading and particle size, a series of Au/CeO_{2-x} catalysts was prepared using controlled variations, including replicate syntheses, co-variation of Sn and Au concentrations, and adjustments in Sn content while keeping Au constant.

The amount of deposited gold was determined by inductively coupled plasma optical emission spectroscopy (ICP-OES), yielding measured loadings of 5.7 wt% ± 0.08 wt% for sample S3-R (abbreviation for; Au seeding 3 on rotating CeO_{2-x}) and 8.2 wt% ± 0.17 wt% for sample S5-S. For the remaining samples, ICP-OES measurements could not be performed; therefore, theoretical gold loadings, calculated from the precursor quantities used during synthesis, are reported instead. The theoretical values for S3-R and S5-S are 5.5 wt% and 6.9 wt%, respectively. These results indicate that the actual gold loading on the CeO_{2-x} surface was approximately 3.6% higher for S3-R and 18.8% higher for S5-S compared to the theoretical

estimates. This deviation may be attributed to partial loss of the ceria support during the Sn deposition and centrifugation steps, resulting in an increase in gold content relative to the remaining support material.

To examine the size, morphology and loading of Au nanoparticles, HAADF-STEM was conducted. However, distinguishing Au from the CeO_{2-x} support using HAADF contrast alone proved challenging, as intensity variations arising from changes in particle thickness were similar to those typically associated with elemental contrast. Therefore, EDX was employed in STEM mode for all samples to enable clear elemental identification and spatial localisation of both Au and Sn on the CeO_{2-x} surface. The EDX maps confirm the presence of both Au (visualised in red) and Sn (visualised in green) across the support (**Figure 2** and SI 4 **Figure S7**). The HAADF-STEM-EDX images shown correspond to synthesis S6-R, while additional images from the other syntheses are provided in the Supporting Information. In particular, the Sn signal appears broadly distributed, covering nearly the entire surface of the CeO_{2-x} particles. Particle size was determined from STEM-EDX images by measuring individual gold nanoparticle diameters and generating corresponding size distribution histograms. Across all samples, the average gold nanoparticle diameter remains below 7 nm, confirming nanoscale dispersion throughout the catalyst series. The reproducibility of the synthesis method was assessed by comparing three catalysts prepared under identical conditions (S1-S, S2-R, and S3-R). Although all three samples show well-dispersed gold nanoparticles, differences in average size and distribution are evident. S2-R displays the smallest and most uniform particles, while S1-S shows larger particles and a broader distribution, including diameters above 10 nm. S3-R falls in between, with intermediate size and variation. These observations suggest that, although the synthesis reliably yields sub-7 nm gold particles, reproducibility in size and uniformity remains limited, indicating a need for further optimization of the procedure. To investigate how increasing both Sn and Au precursors affects gold loading, samples S4-S (2.9 wt% theoretical loading), S3-R (5.7 wt% ICP-OES), and S5-S (8.2 wt% ICP-OES) were compared. A clear increase in gold surface coverage is observed, confirming that higher precursor amounts lead to higher Au loading. This demonstrates the effectiveness of the seeded growth approach for tuning gold content. Despite this trend, particle size measurements show a mix of particle sizes within each sample, indicating that growth is not yet fully controlled. Additionally, since Sn-only mappings already show high surface Sn coverage, the surface likely provides sufficient nucleation sites. This suggests that increasing Au alone, even without more Sn, could still enhance gold loading. To study the effect of $SnCl_2$ concentration on gold deposition, samples S3-R (0.77 eq Sn), S6-R (1.54 eq Sn), and S7-S (4.30 eq Sn) were synthesized with the same

amount of $HAuCl_4$ (0.05 eq). EDX maps show no clear increase in Au surface coverage with rising Sn content, and no change in Sn signal is observed. This aligns with the findings discussed above, suggesting that the CeO_{2-x} surface is already saturated with Sn at lower concentrations. Au particle sizes are comparable within experimental uncertainty: 5.36 ± 1.87 nm (S3-R), 4.38 ± 1.69 nm (S6-R), and 5.07 ± 1.72 nm (S7-S). More systematic and controlled studies using lower Sn concentrations and varied Au amounts are needed to better control gold size and loading, as the current dataset does not allow definitive conclusions about these trends. Based on the STEM-EDX images, the average distance between gold nanoparticles in all plasmonic Au/CeO_{2-x} catalysts is greater than the threshold required for plasmonic coupling. This means that coupling between localized surface plasmons does not occur. Plasmonic coupling typically arises when the gap between adjacent particles is less than approximately half the particle diameter, allowing their electromagnetic fields to interact.[24,25] When this happens, hybridization of plasmon modes leads to a redshift and broadening of the LSPR band.

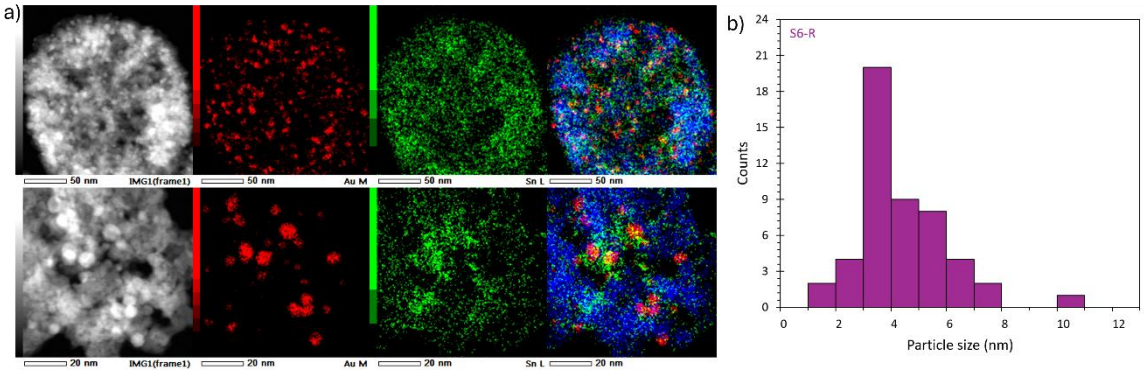

Figure 2. a) Typical HAADF-STEM image and corresponding STEM-EDX elemental maps of S6-R with a theoretical gold loading of 5,5 wt%. In the EDX mapping, Ce is shown in blue, Sn in green, and Au in red. b) Histogram of gold nanoparticle size distribution for S6-R, determined from STEM-EDX images. The data shows an average particle size 4,38 ± 1,69.

Table 2. Particle size and standard deviation for the various Au/CeO_{2-x} catalysts and minimum position of the plasmonic absorption band based on diffuse reflectance UV-Vis spectroscopy.

Au/CeO_{2-x} catalyst:	S1-S	S2-R	S3-R	S4-S	S5-S	S6-R	S7-S
Particle size (nm)	6.77 ± 2.13	4.35 ± 1.16	5.36 ± 1.87	3.23 ± 1.04	4.21 ± 1.12	4.38 ± 1.69	5.07 ± 1.72
Plasmonic absorption band minimum (nm)	528	546	544	544	538	544	544

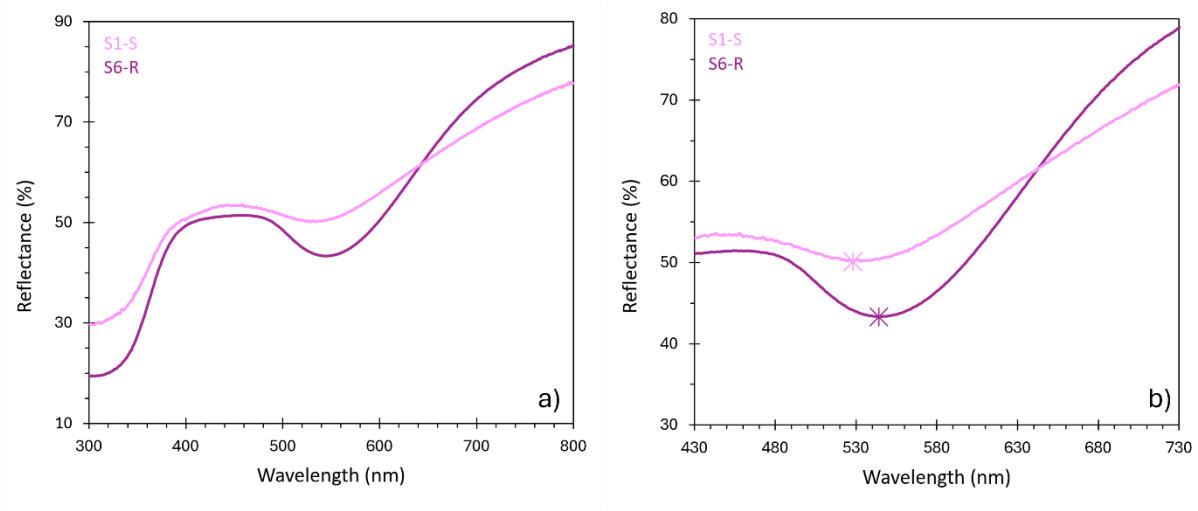

Figure 3. a) Diffuse reflectance UV-Vis spectra of S1-S and S6-R. b) Zoomed-in diffuse reflectance UV-Vis spectra of S1-S and S6-R, highlighting the plasmonic absorption band. The LSPR minima are marked with a star.

Diffuse reflectance UV-Vis spectroscopy was used to investigate the plasmonic properties of the Au/CeO_{2-x} samples. All spectra exhibit a characteristic plasmonic absorption band associated with metallic gold, typically centred between 530 and 600 nm (**Figure 3**, **Table 2** and SI 5 **Figure S8**). Among all samples, only S1-S displays a noticeably broader LSPR band, while the spectra of the remaining catalysts appear quite similar in shape and position. Therefore, only S1-S and S6-R are shown in the main figure for clarity, as the others closely resemble the spectrum of S6-R. Notably, sample S1-S exhibits a slight blue shift in its plasmonic absorption minimum (528 nm) compared to S6-R (544 nm), despite having larger Au particles. The reproduction syntheses S2-R and S3-R, prepared under the same conditions as S1-S, show minima similar to S6-R. We currently have no clear explanation for this observation. The diffuse reflectance UV-Vis spectra reveal a noticeable shift in the absorption band edge when comparing R-CeO_{2-x} to the Au/CeO_{2-x} catalysts. While R-CeO_{2-x} shows an absorption around ~410 nm, all Au/CeO_{2-x} catalysts exhibit a shift toward shorter wavelengths (~370-390 nm), indicating a blue shift in the absorption edge (SI 5 **Figure S8b**). This suggests an apparent increase in bandgap energy upon gold deposition. Tauc analysis was attempted for the Au/CeO_{2-x} catalysts to estimate their optical bandgaps. However, unexpectedly lower bandgap values were obtained at lower wavelengths, which is contrary to the typical behaviour where higher-energy (shorter-wavelength) absorption corresponds to larger bandgaps. This irregularity likely stems from the overlap between the strong plasmonic absorption band of Au and the intrinsic CeO_{2-x} absorption edge. The plasmonic background interferes with the baseline of the Tauc plot, making accurate extrapolation unreliable. Furthermore, the LSPR minima

occur at approximately the same wavelength for all samples, indicating that no redshift is observed. This suggests that the average interparticle spacing is too large to allow for significant plasmon-plasmon coupling, which is consistent with the interparticle distances observed in the STEM-EDX images.

3.3. Plasmon catalysis

3.3.1. Impact of Au loading on catalytic performance

Photocatalytic testing of the Au/CeO_{2-x} materials for the light-driven rWGS reaction was carried out according to the procedure detailed in the experimental section. For all experiments, CO was the only reaction product detected under all tested conditions; no formation of CH_4 was observed. The catalytic activity of unmodified R-CeO_{2-x}, S6-R (5.5 wt% Au and 4.8 ± 1.69 nm) and S7-S (5.5 wt% Au and 5.07 ± 1.72 nm) was investigated and compared with the catalytic activity of Au/CeO_{2-x} (3.67 wt% Au and 8.27 ± 3.10 nm) by Volders (V-) et al[12] and Au/TiO_2 (2.95 wt% Au and 1.6-1.7 nm) by Sastre (S-) et al.[26] (**Figure 4** and **Table 3**).

The unmodified R-CeO_{2-x} support showed no measurable photocatalytic activity under light irradiation alone. However, a very minor amount of CO was produced when the support was externally heated to 250 ºC under simultaneous illumination and without illumination.

All modified catalysts display low activity under illumination alone (9 suns) without external heating. Upon increasing the temperature to 150 ºC and further to 250 ºC under illumination, a significant enhancement in CO production rate is observed across all catalysts, showing that thermal input is essential for achieving high catalytic activity. When the light is turned off while maintaining the temperature at 250 ºC, the CO production rate drops substantially. However, the activity does not fall back to the baseline level observed under room-temperature illumination alone. For the remainder of this discussion, we will focus only on the "light off + 250 ºC" and "light on + 250 ºC" conditions

Under thermal conditions (250 ºC, light off), both S7-S and S6-R exhibit similar CO production rates. This comparable performance can be attributed to their equivalent theoretical Au loading and similar Au particle sizes. Nonetheless, both catalysts are significantly less active than Volders' Au/CeO_{2-x} system (~1.2x higher activity), and especially Sastre's Au/TiO_2, which shows a markedly higher activity (~14x).

The relatively low activity of S6-R and S7-S compared to V-Au/CeO_{2-x} may be attributed to Sn loading, since the particle size of the Au particles of Volders is higher. Although Sn^{2+} facilitates partial reduction of Ce^{4+} to Ce^{3+}, excessive surface coverage by Sn might hinder catalytic activity. Overloading may result in the masking of catalytically active Ce^{3+} sites and

V_os, both of which are essential for CO_2 activation. Ce^{3+} plays a central role in the redox cycle, enabling electron donation to adsorbed CO_2 species and stabilising intermediates necessary for CO formation.

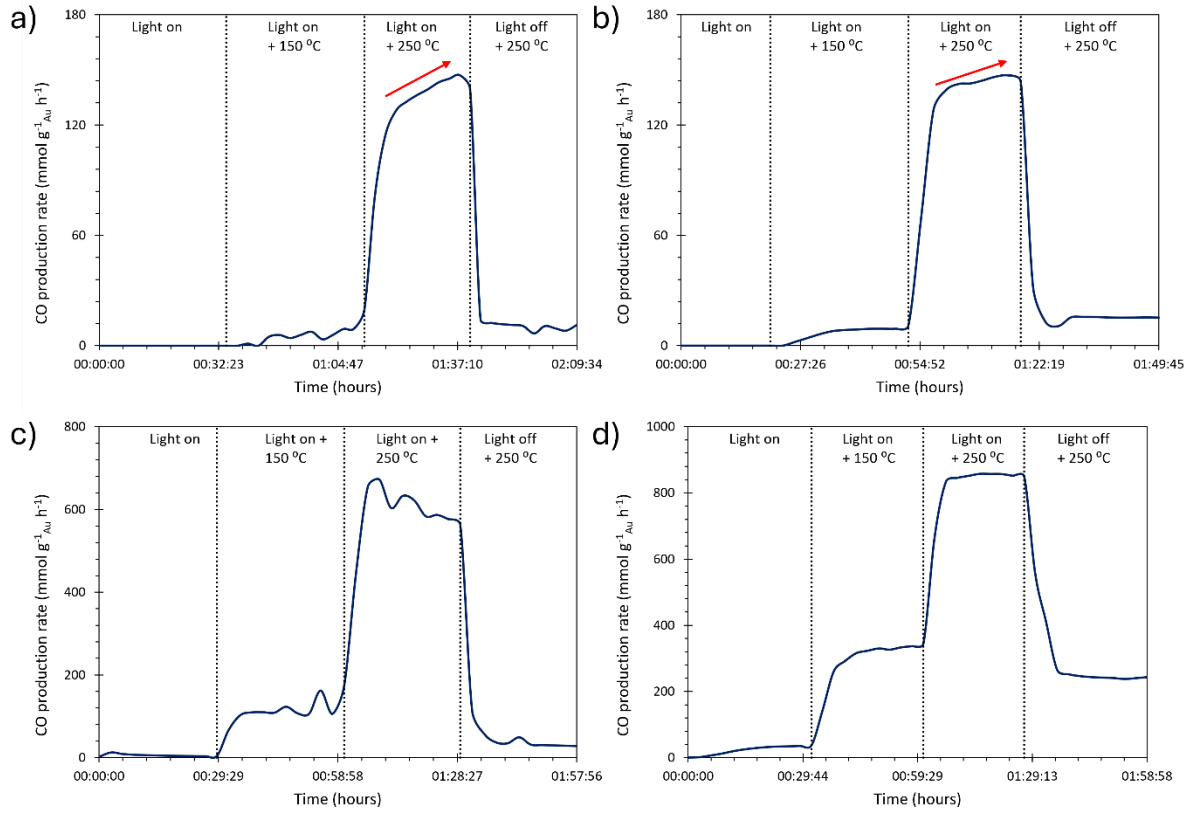

Figure 4. CO production profiles for (a) 5,5 wt% Au S6-R, (b) 5,5 wt% Au S7-S, (c) 3.6 wt% Au on CeO_{2-x} synthesised following the method of Volders et al., and (d) 2.97 wt% Au on TiO_2 synthesised according to Sastre et al. The plasmonic photocatalytic tests were carried out under four sequential conditions: 30 minutes of light irradiation only, followed by 30 minutes of combined irradiation and heating at 150 ºC, then 30 minutes of irradiation at 250 ºC, and finally 30 minutes of thermal treatment at 250 ºC in the absence of light.

Table 3. CO production rates 5,5 wt% Au S6-R, 5,5 wt% Au S7-S, 3.6 wt% Au on CeO_{2-x} synthesised following the method of Volders et al., and 2.97 wt% Au on TiO_2 synthesised according to Sastre et al.

Catalyst	Light on + RT ($mmol\ g^{-1}_{Au}\ h^{-1}$)	Light on + 150 ºC ($mmol\ g^{-1}_{Au}\ h^{-1}$)	Light on + 250 ºC ($mmol\ g^{-1}_{Au}\ h^{-1}$)	Light off + 250 ºC ($mmol\ g^{-1}_{Au}\ h^{-1}$)
S6-R	0,00 ± 0,00	6,27 ± 2,03	142,34 ± 4,37	10,32 ± 1,84
S7-S	0,00 ± 0,00	8,79 ± 0,52	144,55 ± 2,09	15,38 ± 0,13
V-Au/CeO_{2-x}	4,20 ± 0,48	116,62 ± 19,23	616,44 ± 35,16	33,82 ± 6,95
S-Au/TiO_2	32,70 ± 2,50	327,60 ± 7,65	850,65 ± 8,18	243,23 ± 4,44

The comparatively lower performance of Au/CeO_{2-x} under thermal (dark) conditions, relative to Au/TiO_2, can be attributed to the strong binding of CO at oxygen vacancy sites on CeO_{2-x}.[13,27] These vacancies, while beneficial for CO_2 reduction, can also act as product sinks by stabilizing CO too strongly, thereby hindering desorption. TiO_2, with fewer and less reactive oxygen vacancies, enables more facile CO desorption under thermal conditions.

The catalytic CO production rates at 250 ºC under light irradiation are significantly higher than those measured without illumination for all catalysts. Improved performance in photocatalytic experiments compared to thermal-only conditions arises from the combined effects of e.g. photogenerated charge carriers and localized photothermal heating. However, the magnitude of enhancement varies between systems. For the S6-R and S7-S catalysts, photo-enhancement factors with respect to thermal experiments of approximately 13.8x and 9.4x were calculated, respectively. This effect is even more pronounced for the V-Au/CeO_{2-x} reference catalyst (~18.2x), while the S-Au/TiO_2 system shows the lowest enhancement (~3.5x).

This variation indicates that the extent of photo-enhancement is not solely determined by the presence of plasmonic Au, but is also strongly influenced by the properties of the support material. Reduced CeO_{2-x} appears to benefit more under illumination due to its ability to absorb visible light through oxygen vacancy-induced states, as well as its redox-active Ce^{3+}/Ce^{4+} cycle, which may interact synergistically with hot electrons from Au to promote CO_2 activation. In contrast, TiO_2, despite its wide bandgap and low oxygen storage capacity, exhibits a higher overall thermal performance, though its relative photo-enhancement is less pronounced.

3.3.2. Continuous increase in catalytic performance

Another observation is the gradual increase in CO production rate over time within each measurement condition for the catalysts of this study compared to the reference. Steady-state conditions are not reached within the duration of each measurement step. This behaviour could be related to the progressive activation of V_Os, which may require time under reaction conditions to become catalytically active. The oxidation state of cerium in the CeO_{2-x} support plays a critical role in determining the catalytic activity of Au/CeO_{2-x} catalysts.[12] In thermally oxidized CeO_2, cerium exists predominantly in the Ce^{4+} state, resulting in a fully oxidized lattice with minimal V_Os. As V_Os are key active sites for many catalytic reactions, the lack thereof renders Au/CeO_2 primarily a precatalyst. During catalytic operation, V_Os must first be generated, typically through reduction processes, which delays activity onset and can reduce overall catalytic performance. In contrast, reduced ceria, which contains a higher proportion of Ce^{3+}, inherently possesses more oxygen vacancies and thus provides a more active surface for catalytic processes.

At the same time, it is important to consider the role of Sn^{2+}, which is introduced to facilitate gold nanoparticle nucleation. Sn^{2+} can also promote the reduction of Ce^{4+} to Ce^{3+}, thereby increasing the initial concentration of oxygen vacancies. This raises the question of why a gradual activation is still observed if vacancy sites are already present. One possible explanation is that while Sn^{2+} enhances reducibility locally, it may also partially block or occupy surface sites, thereby limiting their catalytic accessibility at the start of the reaction.

3.3.3. Catalyst stability

A clear colour change was observed for the S7-S catalyst after plasmonic catalysis, shifting from purple to green. This change is accompanied by a notable alteration in the DR-UV-Vis spectrum (SI5 **Figure S9**), where the plasmonic absorption band becomes less pronounced after the reaction. Such spectral changes suggest modifications in the surface or structural properties of the catalyst. Possible explanations include agglomeration or reshaping of gold nanoparticles, oxidation state changes in gold or ceria, or alterations in the density of oxygen vacancies. As the other catalysts did not show this behaviour, it points to a stability issue specific to S7-S. Further studies are necessary to identify the exact cause of this transformation and its potential effect on catalytic performance.

4. Conclusion

In summary, hydrothermal synthesis of CeO_{2-x} under both rotating and static conditions yielded phase-pure, cubic fluorite-structured nanoparticles with similar mean particle sizes (~120 nm). However, rotation significantly reduced size variability, likely due to enhanced temperature and solute homogeneity. Crystallite sizes (~20 nm) remained unaffected by rotation, suggesting minimal impact on primary crystallite growth. TEM analysis revealed consistent morphology across methods, while XRD confirmed structural purity with no phase impurities or peak shifts. Optical characterization of R-CeO_{2-x} revealed a band gap of ~3.0 eV, consistent with known ceria properties. Overall, autoclave rotation offers a simple yet effective means to enhance particle size uniformity.

Gold was deposited onto both S- and R-CeO_{2-x} supports using a seeded growth method involving Sn^{2+} pre-treatment and chemical reduction with formaldehyde. STEM-EDX mapping confirmed homogeneous Sn surface coverage and localized gold nucleation across all samples. Average gold particle sizes remained below 7 nm, indicating good dispersion, although reproducibility in particle size and uniformity remains limited. Tuning the Au and Sn precursor amounts showed that gold loading increases with increasing precursor concentration, as verified by ICP-OES and supported by STEM-EDX imaging. However, particle growth remains only

partially controlled, with size distributions varying within samples. Further increasing Sn alone did not significantly impact gold size and distribution, likely due to surface saturation with Sn. The diffuse reflectance UV-Vis spectra confirmed consistent plasmonic absorption across all catalysts, with no evidence of plasmon coupling, as interparticle distances exceeded the coupling threshold.

The plasmonic Au/CeO_{2-x} catalysts demonstrated clear photocatalytic activity for the light-assisted rWGS reaction, with CO as the sole product. Unmodified CeO_{2-x} showed almost no measurable activity, confirming the necessity of gold for catalytic function. Among the prepared catalysts, S6-R and S7-S (both 5.5 wt% Au) exhibited moderate performance but remained significantly less active than benchmark systems such as V-Au/CeO_{2-x} and S-Au/TiO_2. This reduced activity, despite similar Au particle sizes, may be attributed to excess Sn^{2+}. While Sn^{2+} promotes gold deposition and enhances reducibility by converting Ce^{4+} to Ce^{3+}, it may also block active surface sites such as V_os, which are essential for CO_2 reduction.

All CeO_{2-x} based catalysts displayed a substantial photo-enhancement in CO production under illumination, with factors of ~13.8x (S6-R) and ~9.4x (S7-S). This enhancement arises not only from the plasmonic properties of Au but also from the redox-active CeO_{2-x} support. Its visible-light absorption and Ce^{3+}/Ce^{4+} redox cycling enable synergistic interactions with hot electrons from Au, thereby promoting photocatalytic CO_2 reduction. In contrast, TiO_2 exhibited higher baseline thermal activity but lower photo-enhancement (~3.5x), reflecting the limited contribution of its support under light irradiation.

A gradual increase in activity over time was observed for all CeO_{2-x}-based catalysts, suggesting a transformation from an initially inactive, Ce^{4+}-rich precatalyst into a more active state as oxygen vacancies become accessible during the reaction. This activation process, even in the presence of Sn^{2+}, points to dynamic restructuring of the catalyst surface.

Post-reaction analysis revealed degradation of the S7-S Au/CeO_{2-x} catalyst, including a colour change and diminished plasmonic absorption, likely due to gold agglomeration or alteration of the support. This highlights the need to further investigate catalyst stability under operating conditions.

To further optimize the plasmonic Au/CeO_{2-x} catalysts, future experiments should explore the effect of increasing the ratio of Au with respect to Sn, as well as reducing the Sn concentration compared to the current synthesis. These adjustments may allow for better control over gold loading and size. Moreover, the influence of Sn on the generation and accessibility of V_os should be systematically investigated. Hydrogen temperature-programmed reduction (H_2-TPR) is a valuable tool for this purpose, as it enables indirect quantification of oxygen

vacancy concentrations through analysis of ceria reducibility. This technique would help clarify whether Sn reduces the formation of catalytically active surface vacancies, as is currently assumed.

Although enhanced CO production was observed under illumination, this cannot be conclusively attributed to a purely photothermal effect. Non-thermal mechanisms, such as direct photoexcitation or hot electron transfer, may also contribute, or act in combination. Further experimental work is needed to verify this, for example by evaluating the catalytic activity as a function of light intensity, using wavelength-selective filters, or implementing accurate in-situ temperature measurements inside the catalyst bed. These studies are essential to distinguish between thermal and non-thermal contributions and to gain a deeper understanding of the underlying mechanisms of plasmon-enhanced catalysis.

Acknowledgements

I would like to begin by sincerely thanking my promoters, Prof. Dr. Pascal Buskens and Prof. Dr. Marlies Van Bael, whose guidance and encouragement have been instrumental throughout this project. Their support played a key role in shaping both the progress and the learning journey that came with it.

I am also grateful to the DESINe group's PC team for the many stimulating conversations and idea exchanges that enriched my laboratory work. Beyond the contributions of my promoters, I particularly want to acknowledge Ms. Esmee Roman, Dr. Daniel Mann, and Dr. Ken Elen for their valuable insights and collaboration.

A heartfelt thank-you goes out to all the researchers who performed essential analyses on my samples, supplying critical data for this thesis. These include Dr. Marcel A. Verheijen for HAADF-STEM-EDX, Mr. Digvijay Ghogare for ICP-OES, and Ms. Nele Debusschere, Ms. Naomi Billiet, and Ms. Hanne Broux for XRD measurements. I also appreciate the TEM work carried out by Mr. Sander Stulens and Ms. Esmee Roman.

Lastly, I want to give special recognition to Ir. Thomas Vranken for his dedicated help and technical expertise with the plasmon reactor.

References

(1) Calvin, K.; Dasgupta, D.; et al. *IPCC, 2023: Climate Change 2023: Synthesis Report. Contribution of Working Groups I, II and III to the Sixth Assessment Report of the Intergovernmental Panel on Climate Change. IPCC, Geneva, Switzerland.*; 2023. https://doi.org/10.59327/IPCC/AR6-9789291691647.

(2) Osman, A. I.; Hefny, M.; Abdel Maksoud, M. I. A.; Elgarahy, A. M.; Rooney, D. W. Recent Advances in Carbon Capture Storage and Utilisation Technologies: A Review. *Environ Chem Lett* **2021**, *19* (2), 797–849. https://doi.org/10.1007/s10311-020-01133-3.

(3) Xiao, Z.; Li, P.; Zhang, H.; Zhang, S.; Tan, X.; Ye, F.; Gu, J.; Zou, J.; Wang, D. A Comprehensive Review on Photo-Thermal Co-Catalytic Reduction of CO2 to Value-Added Chemicals. *Fuel* **2024**, *362*, 130906. https://doi.org/10.1016/j.fuel.2024.130906.

(4) Fresno, F.; Iglesias-Juez, A.; Coronado, J. M. Photothermal Catalytic CO2 Conversion: Beyond Catalysis and Photocatalysis. *Top Curr Chem* **2023**, *381* (4), 21. https://doi.org/10.1007/s41061-023-00430-z.

(5) Kaiser, P.; Unde, R. B.; Kern, C.; Jess, A. Production of Liquid Hydrocarbons with CO $_2$ as Carbon Source Based on Reverse Water-Gas Shift and Fischer-Tropsch Synthesis. *Chemie Ingenieur Technik* **2013**, *85* (4), 489–499. https://doi.org/10.1002/cite.201200179.

(6) Volders, J.; Elen, K.; Raes, A.; Ninakanti, R.; Kelchtermans, A.-S.; Sastre, F.; Hardy, A.; Cool, P.; Verbruggen, S. W.; Buskens, P.; Van Bael, M. K. Sunlight-Powered Reverse Water Gas Shift Reaction Catalysed by Plasmonic Au/TiO2 Nanocatalysts: Effects of Au Particle Size on the Activity and Selectivity. *Nanomaterials* **2022**, *12* (23), 4153. https://doi.org/10.3390/nano12234153.

(7) Sastre, F.; Versluis, C.; Meulendijks, N.; Rodríguez-Fernández, J.; Sweelssen, J.; Elen, K.; Van Bael, M. K.; den Hartog, T.; Verheijen, M. A.; Buskens, P. Sunlight-Fueled, Low-Temperature Ru-Catalyzed Conversion of CO_2 and H_2 to CH_4 with a High Photon-to-Methane Efficiency. *ACS Omega* **2019**, *4* (4), 7369–7377. https://doi.org/10.1021/acsomega.9b00581.

(8) Li, X.; Yu, J.; Jaroniec, M.; Chen, X. Cocatalysts for Selective Photoreduction of CO_2 into Solar Fuels. *Chem Rev* **2019**, *119* (6), 3962–4179. https://doi.org/10.1021/acs.chemrev.8b00400.

(9) Baffou, G.; Bordacchini, I.; Baldi, A.; Quidant, R. Simple Experimental Procedures to Distinguish Photothermal from Hot-Carrier Processes in Plasmonics. *Light Sci Appl* **2020**, *9* (1), 108. https://doi.org/10.1038/s41377-020-00345-0.

(10) Lu, B.; Quan, F.; Sun, Z.; Jia, F.; Zhang, L. Photothermal Reverse-Water-Gas-Shift over Au/CeO2 with High Yield and Selectivity in CO2 Conversion. *Catal Commun* **2019**, *129*, 105724. https://doi.org/10.1016/j.catcom.2019.105724.

(11) Upadhye, A. A.; Ro, I.; Zeng, X.; Kim, H. J.; Tejedor, I.; Anderson, M. A.; Dumesic, J. A.; Huber, G. W. Plasmon-Enhanced Reverse Water Gas Shift Reaction over Oxide

Supported Au Catalysts. *Catal Sci Technol* **2015**, *5* (5), 2590–2601. https://doi.org/10.1039/C4CY01183J.

(12) Volders, J.; Bossier, S.; Stulens, S.; Joos, B.; Vranken, T.; Sastre, F.; D'Haen, J.; Elen, K.; Verheijen, M. A.; Cool, P.; Hardy, A.; Buskens, P.; Van Bael, M. K. The Influence of Size, Metal Loading and Oxygen Vacancies on the Catalytic Performance of Au/CeO2 in the Sunlight-Powered Reverse Water Gas Shift Reaction. *Catal Sci Technol* **2025**, *15* (2), 486–500. https://doi.org/10.1039/D4CY01194E.

(13) Ebrahimi, P.; Kumar, A.; Khraisheh, M. A Review of CeO2 Supported Catalysts for CO2 Reduction to CO through the Reverse Water Gas Shift Reaction. *Catalysts* **2022**, *12* (10), 1101. https://doi.org/10.3390/catal12101101.

(14) TROVARELLI, A. Catalytic Properties of Ceria and CeO_2 -Containing Materials. *Catalysis Reviews* **1996**, *38* (4), 439–520. https://doi.org/10.1080/01614949608006464.

(15) da Silva, A. G. M.; Rodrigues, T. S.; Wang, J.; Camargo, P. H. C. Plasmonic Catalysis with Designer Nanoparticles. *Chemical Communications* **2022**, *58* (13), 2055–2074. https://doi.org/10.1039/D1CC03779J.

(16) Mann, D.; Nascimento-Duplat, D.; Keul, H.; Möller, M.; Verheijen, M.; Xu, M.; Urbach, H. P.; Adam, A. J. L.; Buskens, P. The Influence of Particle Size Distribution and Shell Imperfections on the Plasmon Resonance of Au and Ag Nanoshells. *Plasmonics* **2017**, *12* (3), 929–945. https://doi.org/10.1007/s11468-016-0345-8.

(17) Wang, Q.; Jia, W.; Liu, B.; Zhao, W.; Li, C.; Zhang, J.; Xu, G. Controllable Synthesis of Nearly Monodisperse Spherical Aggregates of CeO_2 Nanocrystals and Their Catalytic Activity for HCHO Oxidation. *Chem Asian J* **2012**, *7* (10), 2258–2267. https://doi.org/10.1002/asia.201200432.

(18) Nadjia, L.; Abdelkader, E.; Naceur, B.; Ahmed, B. CeO2 Nanoscale Particles: Synthesis, Characterization and Photocatalytic Activity under UVA Light Irradiation. *Journal of Rare Earths* **2018**, *36* (6), 575–587. https://doi.org/10.1016/j.jre.2018.01.004.

(19) Jin, S.; Guan, X.; Zhang, X.; Zhang, C.; Liu, J.; Wang, Y.; Wang, Y.; Li, R.; Li, Z.; Fan, C. CeO2 Nanorods with Bifunctional Oxygen Vacancies for Promoting Low-Pressure Photothermocatalytic CO2 Conversion with CH3OH to Dimethyl Carbonate. *J Environ Chem Eng* **2023**, *11* (6), 111374. https://doi.org/10.1016/j.jece.2023.111374.

(20) Gonzalez Castaño, M.; Reina, T. R.; Ivanova, S.; Centeno, M. A.; Odriozola, J. A. Pt vs. Au in Water–Gas Shift Reaction. *J Catal* **2014**, *314*, 1–9. https://doi.org/10.1016/j.jcat.2014.03.014.

(21) Petrovsky, V.; Gorman, B. P.; Anderson, H. U.; Petrovsky, T. Optical Properties of CeO2 Films Prepared from Colloidal Suspension. *J Appl Phys* **2001**, *90* (5), 2517–2521. https://doi.org/10.1063/1.1389329.

(22) Zhao, Y.; Teng, B.; Yang, Z.; Zhao, Y.; Zhao, L.; Luo, M. Density Functional Theory Study of Sn Adsorption on the CeO2 Surface. *The Journal of Physical Chemistry C* **2011**, *115* (33), 16461–16466. https://doi.org/10.1021/jp203640f.

(23) Škoda, M.; Cabala, M.; Cháb, V.; Prince, K. C.; Sedláček, L.; Skála, T.; Šutara, F.; Matolín, V. Sn Interaction with the CeO2(111) System: Bimetallic Bonding and Ceria Reduction. *Appl Surf Sci* **2008**, *254* (14), 4375–4379. https://doi.org/10.1016/j.apsusc.2008.01.080.

(24) Jain, P. K.; El-Sayed, M. A. Plasmonic Coupling in Noble Metal Nanostructures. *Chem Phys Lett* **2010**, *487* (4–6), 153–164. https://doi.org/10.1016/j.cplett.2010.01.062.

(25) Liu, D.; Xue, C. Plasmonic Coupling Architectures for Enhanced Photocatalysis. *Advanced Materials* **2021**, *33* (46). https://doi.org/10.1002/adma.202005738.

(26) Martínez Molina, P.; Meulendijks, N.; Xu, M.; Verheijen, M. A.; den Hartog, T.; Buskens, P.; Sastre, F. Low Temperature Sunlight-Powered Reduction of CO2 to CO Using a Plasmonic Au/TiO2 Nanocatalyst. *ChemCatChem* **2021**, *13* (21), 4507–4513. https://doi.org/10.1002/cctc.202100699.

(27) Bolarinwa, M. O.; Dabbawala, A. A.; Talib, S. H.; Melinte, G.; Delclos, T.; Adamson, A.; Khaleel, A.; Polychronopoulou, K.; Anjum, D. H. High-Performance Single-Atom M/TiO2 Catalysts in the Reverse Water-Gas Shift Reaction: A Comprehensive Experimental and Theoretical Investigation. *Journal of CO2 Utilization* **2024**, *90*, 102988. https://doi.org/10.1016/j.jcou.2024.102988.

Supporting information

SI 1: Au seeding on CeO_{2-x} support

Table S4. Au seeding 1 on CeO_{2-x} support. Theoretical gold content is 5.5 wt%.

Reagent	Amount	MW (g/mol)	Moles (mol)	Equivalents (vs. CeO_{2-x})
STEP 1				
CeO_{2-x}	49,8 mg	172,11	289,35	1,0
Milli-Q	2 mL	x	x	x
STEP 2				
$SnCl_2$	41,9 mg	189,60	220,99	0,76
HCl (37%)	100 µL	x	x	x
Milli-Q	20 mL	x	x	x
STEP 3				
$HAuCl_4 * x\ H_2O$	5 mg	339,79	14,71	0,05
K_2CO_3	5 mg	138,21	36,18	0,13
Milli-Q	20 mL	x	x	x
STEP 4				
CH_2O (37%)	5,41 mL	x	x	x

Table S5. Au seeding 2 on CeO_{2-x} support. Theoretical gold content is 5.5 wt%.

Reagent	Amount	MW (g/mol)	Moles (mol)	Equivalents (vs. CeO_{2-x})
STEP 1				
CeO_{2-x}	49,6 mg	172,11	288,19	1,0
Milli-Q	2 mL	x	x	x
STEP 2				
$SnCl_2$	42 mg	189,60	221,52	0,77
HCl (37%)	100 µL	x	x	x
Milli-Q	20 mL	x	x	x
STEP 3				
$HAuCl_4 * x\ H_2O$	5 mg	339,79	14,71	0,05
K_2CO_3	5 mg	138,21	36,18	0,13
Milli-Q	20 mL	x	x	x
STEP 4				
CH_2O (37%)	5,41 mL	x	x	x

Table S6. Au seeding 3 on CeO_{2-x} support. Theoretical gold content is 5.5 wt%.

Reagent	Amount	MW (g/mol)	Moles (mol)	Equivalents (vs. CeO_{2-x})
STEP 1				
CeO_{2-x}	197,3 mg	172,11	1146,36	1,0
Milli-Q	8 mL	x	x	x
STEP 2				
$SnCl_2$	168 mg	189,60	886,08	0,77
HCl (37%)	400 µL	x	x	x
Milli-Q	80 mL	x	x	x
STEP 3				
$HAuCl_4 * x\ H_2O$	20 mg	339,79	58,86	0,05
K_2CO_3	20 mg	138,21	144,71	0,13
Milli-Q	80 mL	x	x	x
STEP 4				
CH_2O (37%)	21,64 mL	x	x	x

Table S7. Au seeding 4 on CeO_{2-x} support. Theoretical gold content is 2,9 wt%.

Reagent	Amount	MW (g/mol)	Moles (mol)	Equivalents (vs. CeO_{2-x})
STEP 1				
CeO_{2-x}	197,1 mg	172,11	1145,20	1,0
Milli-Q	8 mL	x	x	x
STEP 2				
$SnCl_2$	84 mg	189,60	443,03	0,39
HCl (37%)	200 µL	x	x	x
Milli-Q	48 mL	x	x	x
STEP 3				
$HAuCl_4 * x\ H_2O$	10 mg	339,79	29,42	0,03
K_2CO_3	10 mg	138,21	72,35	0,06
Milli-Q	40 mL	x	x	x
STEP 4				
CH_2O (37%)	10,82 mL	x	x	x

Table S8. Au seeding 5 on CeO_{2-x} support. Theoretical gold content is 6,9 wt%.

Reagent	Amount	MW (g/mol)	Moles (mol)	Equivalents (vs. CeO_{2-x})
STEP 1				
CeO_{2-x}	196,6 mg	172,11	1142,29	1,0
Milli-Q	8 mL	x	x	x
STEP 2				
$SnCl_2$	210 mg	189,60	1107,59	0,97
HCl (37%)	500 µL	x	x	x
Milli-Q	100 mL	x	x	x
STEP 3				
$HAuCl_4 * x\ H_2O$	25 mg	339,79	73,57	0,06
K_2CO_3	25 mg	138,21	180,88	0,16
Milli-Q	100 mL	x	x	x
STEP 4				
CH_2O (37%)	27,05 mL	x	x	x

Table S9. Au seeding 6 on CeO_{2-x} support. Theoretical gold content is 5,5 wt%.

Reagent	Amount	MW (g/mol)	Moles (mol)	Equivalents (vs. CeO_{2-x})
STEP 1				
CeO_{2-x}	198,4 mg	172,11	1152,75	1,0
Milli-Q	8 mL	x	x	x
STEP 2				
$SnCl_2$	337 mg	189,60	1777,42	1,54
HCl (37%)	800 µL	x	x	x
Milli-Q	80 mL	x	x	x
STEP 3				
$HAuCl_4 * x\ H_2O$	20 mg	339,79	58,86	0,05
K_2CO_3	20 mg	138,21	144,71	0,13
Milli-Q	80 mL	x	x	x
STEP 4				
CH_2O (37%)	21,64 mL	x	x	x

Table S10. Au seeding 7 on CeO_{2-x} support. Theoretical gold content is 5,5 wt%.

Reagent	Amount	MW (g/mol)	Moles (mol)	Equivalents (vs. CeO_{2-x})
STEP 1				
CeO_{2-x}	199,1 mg	172,11	1156,82	1,0
Milli-Q	8 mL	x	x	x
STEP 2				
$SnCl_2$	942,5 mg	189,60	4970,99	4,30
HCl (37%)	800 µL	x	x	x
Milli-Q	80 mL	x	x	x
STEP 3				
$HAuCl_4 * x\ H_2O$	20 mg	339,79	58,86	0,05
K_2CO_3	20 mg	138,21	144,71	0,13
Milli-Q	80 mL	x	x	x
STEP 4				
CH_2O (37%)	21,64 mL	x	x	x

SI 2: TEM analysis of R-CeO_{2-x} and S-CeO_{2-x}

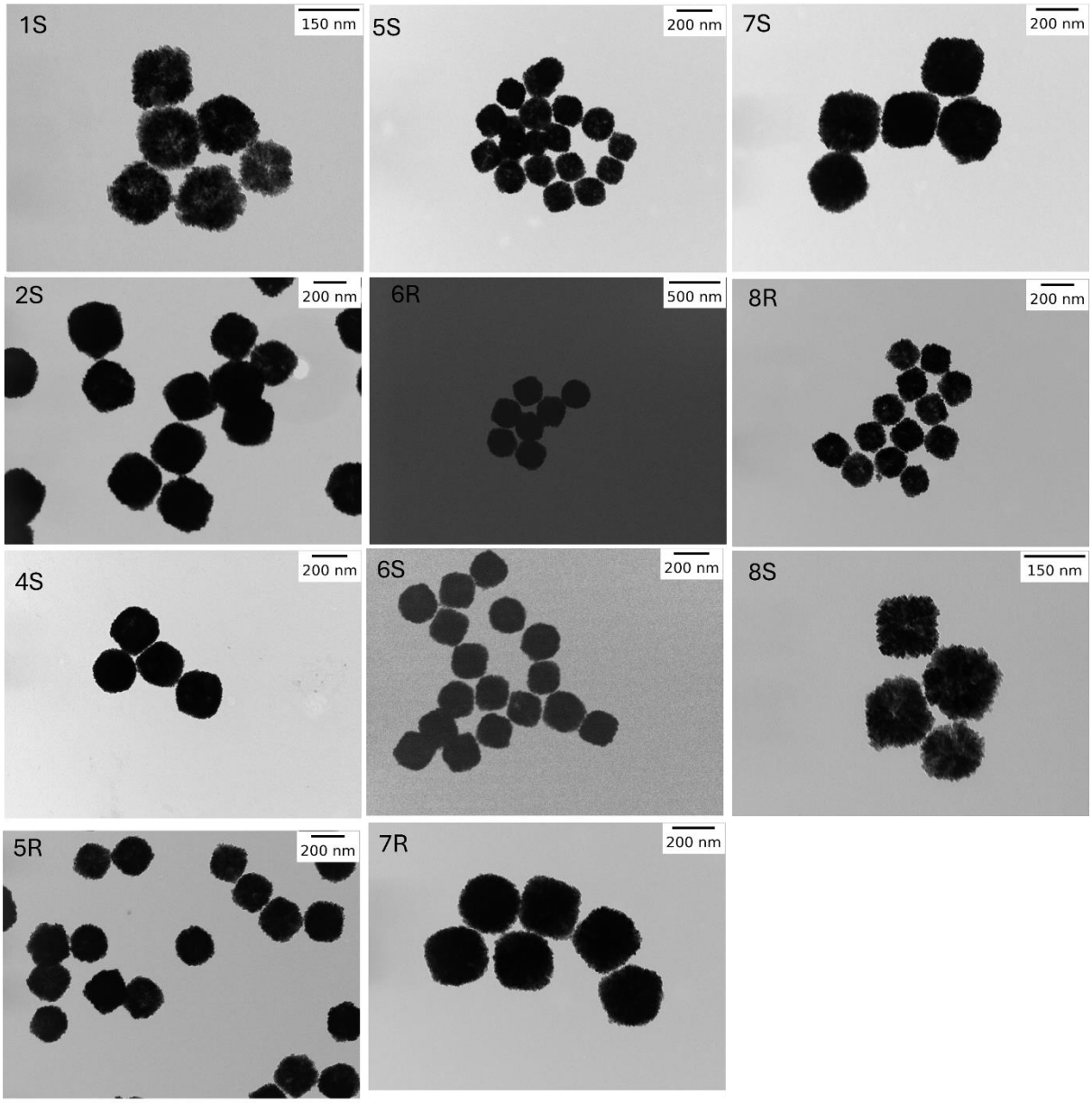

Figure S5. TEM images of R-CeO_{2-x} and S-CeO_{2-x} particles obtained from various hydrothermal syntheses.

SI 3: Tauc analysis on R-CeO_{2-x}

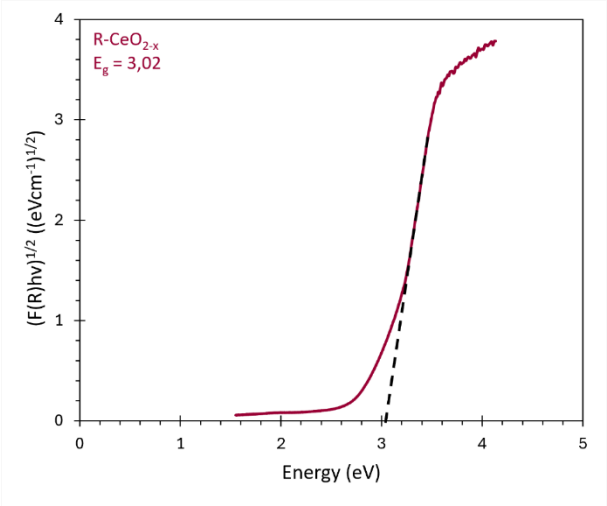

Figure S6. Tauc plot derived from diffuse reflectance UV-Vis data of R-CeO_{2-x} particles. The optical band gap energy was estimated by extrapolating the linear region of the curve to its intersection with the photon energy axis.

SI 4: HAADF-STEM-EDX

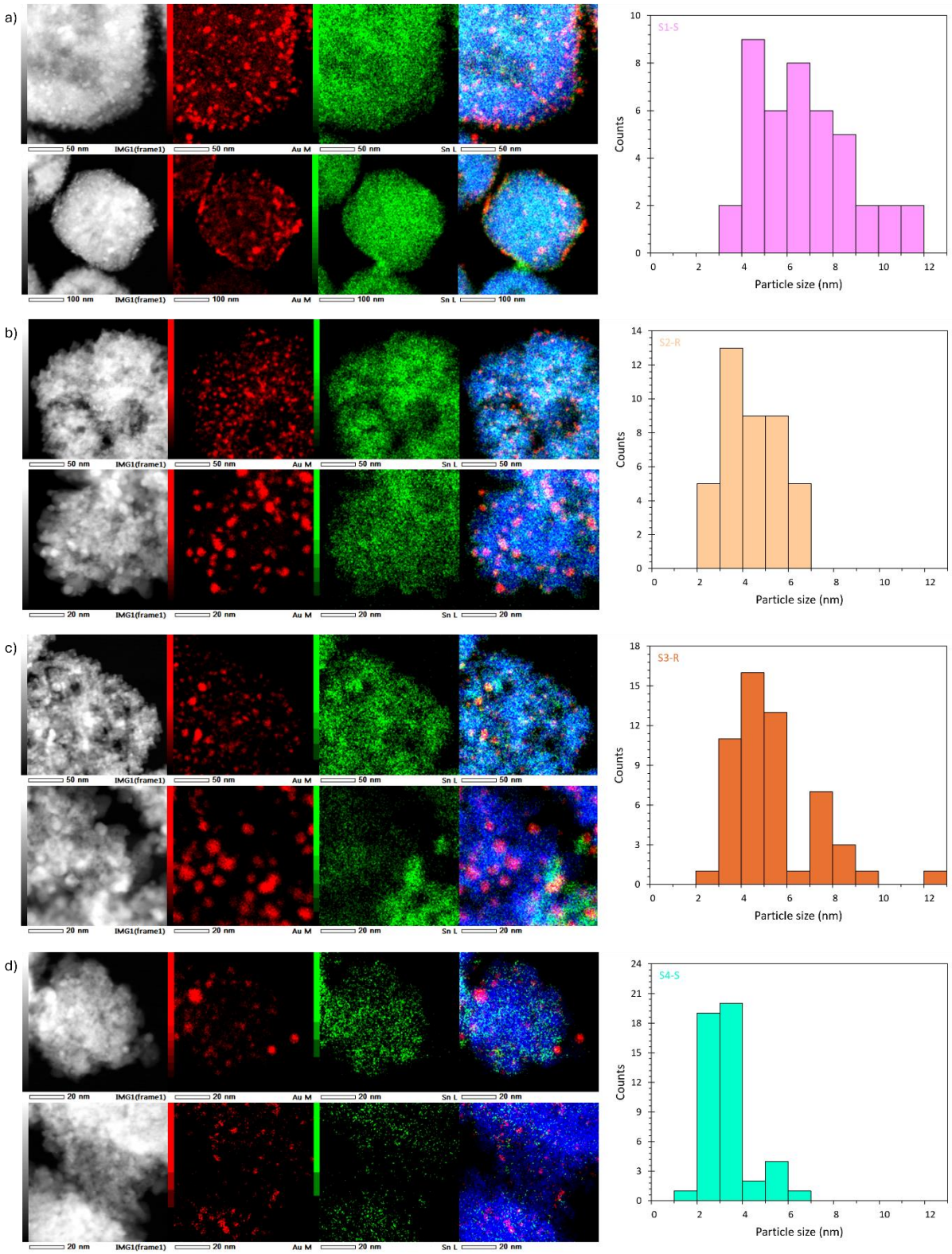

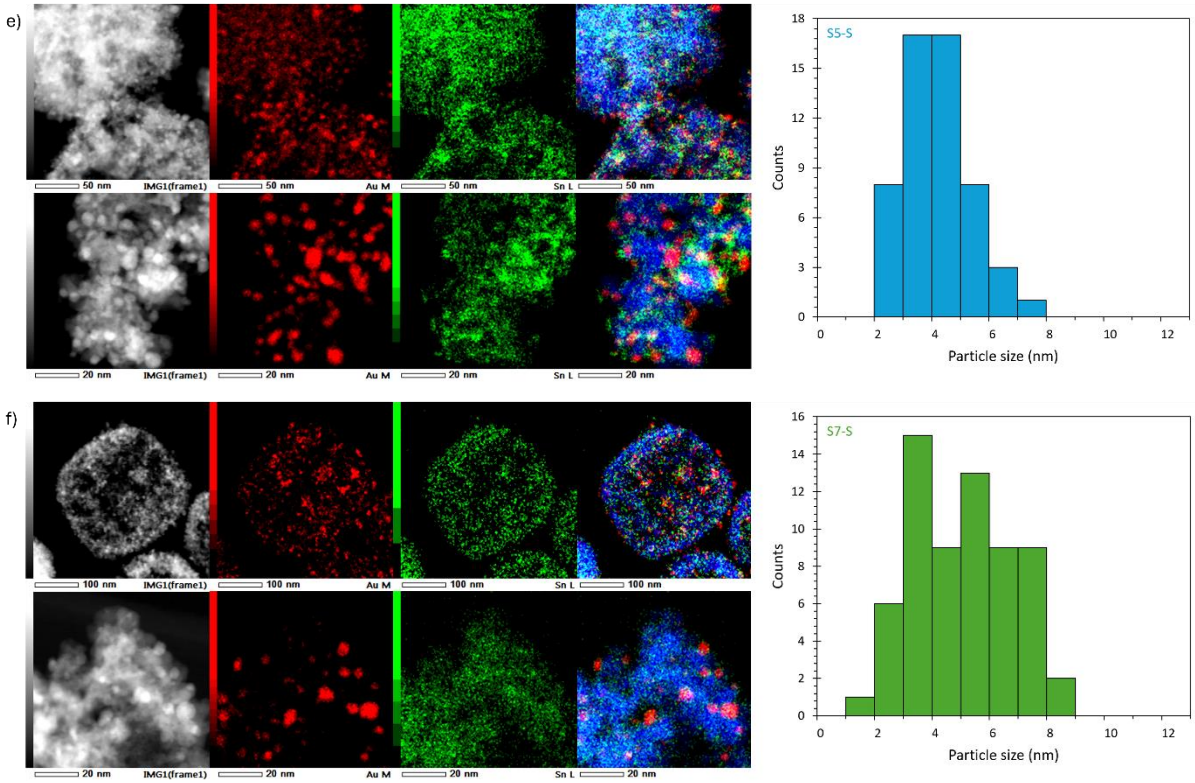

Figure S7. Typical HAADF-STEM image and corresponding STEM-EDX elemental maps of a) S1-S, b) S2-R, c) S3-R, d) S4-S, e) S5-S and f) S7-S. In the EDX mapping, Ce is shown in blue, Sn in green, and Au in red.

SI 5: Diffuse reflectance UV-Vis of Au/CeO_{2-x}

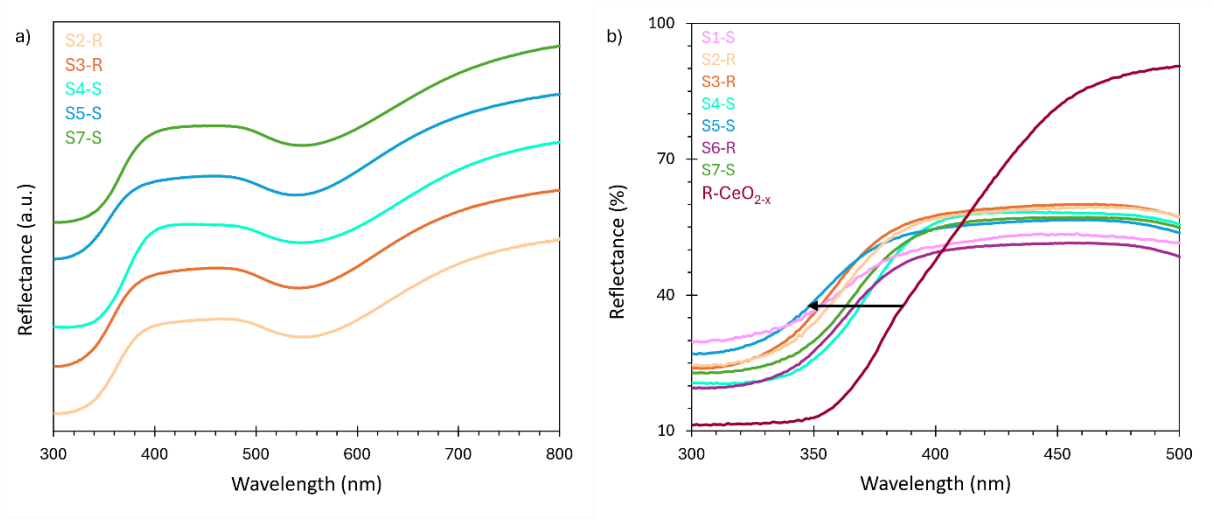

Figure S8. a) Stacked diffuse reflectance UV-Vis spectra of different Au seedings. b) Diffuse reflectance UV-Vis spectra of CeO_{2-x} and all Au seedings showing the bend-edge.

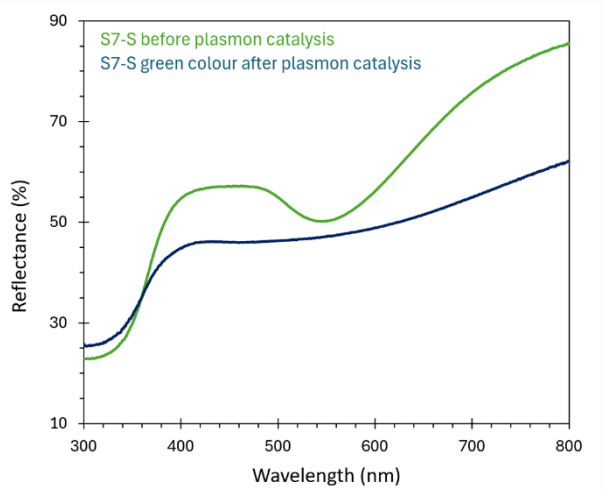

Figure S9. Diffuse reflectance UV-Vis spectra of sample S7-S before and after plasmonic photocatalysis. The catalyst exhibited a noticeable colour change to green following the reaction.

SI 6: Powder XRD from static and rotating hydrothermal synthesis of CeO_{2-x}

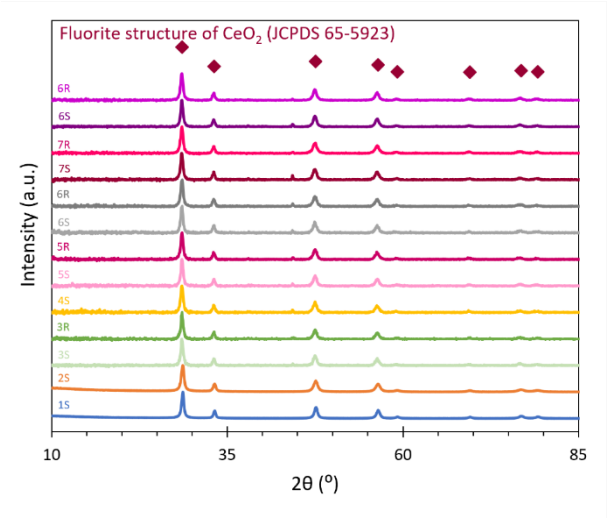

Figure S10. Powder XRD of the different synthesis conducted under static (S) and rotating (R) conditions.